How to cite: Angew. Chem. Int. Ed. 2024, e202401552
doi.org/10.1002/anie.202401552

Photocrystallography

Exploring Pyroelectricity, Thermal and Photochemical Switching in a Hybrid Organic-Inorganic Crystal by In Situ X-Ray Diffraction

*Joshua J. Morris, Chris R. Bowen, Ben A. Coulson, Mark Eaton, Paul R. Raithby, Lucy K. Saunders, Jonathan M. Skelton, Qingping Wang, Mark R. Warren, Yan Zhang, and Lauren E. Hatcher**

Abstract: The switching behavior of the novel hybrid material (FA)Na[Fe(CN)$_5$(NO)].H$_2$O (**1**) in response to temperature (T), light irradiation and electric field (E) is studied using in situ X-ray diffraction (XRD). Crystals of **1** display piezoelectricity, pyroelectricity, second and third harmonic generation. XRD shows that the FA$^+$ are disordered at room-temperature, but stepwise cooling from 273–100 K induces gradual ordering, while cooling under an applied field ($E = +40$ kVcm^{-1}) induces a sudden phase change at 140 K. Structural-dynamics calculations suggest the field pushes the system into a region of the structural potential-energy surface that is otherwise inaccessible, demonstrating that application of T and E offers an effective route to manipulating the crystal chemistry of these materials. Photocrystallography also reveals photoinduced linkage isomerism, which coexists with but is not correlated to other switching behaviors. These experiments highlight a new approach to in situ studies of hybrid materials, providing insight into the structure–property relationships that underpin their functionality.

Introduction

Materials that switch between two or more distinct states on exposure to external stimuli are of importance for a range of technologies including optoelectronics, sensors, high-capacity data-storage, molecular machines and solar energy.[1] Switchable hybrid organic–inorganic crystals have received considerable recent interest, in part due to the myriad proven applications of hybrid perovskite systems such as methylammonium lead iodide (MAPbI$_3$). In particular, piezo-, pyro- and ferroelectric materials have potential applications in the technologies needed to address some of the most pressing global challenges, including energy generation and storage.[2] Hybrid perovskites are archetypal examples, for which the synergy between their ferroelectric switching and light-harvesting capabilities results in favorable properties for applications in next-generation solar cells.[3] However, issues including poor stability, toxicity,[4] and an incomplete understanding of the underlying structure-property mechanisms[5] all necessitate further study.

A pyroelectric response is typically induced by the variation of polarization with temperature (T). However, applying a T-gradient can be a slow process, whereas many real-world applications require a fast or even instantaneous response. Coupling the processes that underpin a pyroelectric response to a fast trigger, e.g. light or an external electric field (E), can in principle facilitate rapid and efficient switching and thus provides a route to the rational design of multifunctional materials with precisely-controlled responses.[1h,6] A route to addressing the need for improved mechanistic insight is to design materials that incorporate a known photoswitch whose light-responsive behavior is al-

[*] J. J. Morris, Dr. B. A. Coulson, Dr. L. E. Hatcher
School of Chemistry
Cardiff University
Main Building, Park Place, Cardiff, CF10 AT, UK
E-mail: HatcherL1@cardiff.ac.uk

Prof. C. R. Bowen, Dr. Q. Wang
Department of Mechanical Engineering
University of Bath
Claverton Down, Bath, BA2 7AY, UK

Dr. M. Eaton
School of Engineering
Cardiff University
Queen's Buildings, The Parade, Cardiff, CF24 3AA, UK

Prof. P. R. Raithby
Department of Chemistry
University of Bath
Claverton Down, Bath, BA2 7AY, UK

Dr. L. K. Saunders, Dr. M. R. Warren
Diamond Light Source
Harwell Science and Innovation Campus, Fermi Ave, Didcot OX11 0DE, UK

Dr. J. M. Skelton
Department of Chemistry
University of Manchester
Oxford Road, Manchester, M13 9PL, UK

Dr. Y. Zhang
State Key Laboratory of Powder Metallurgy
Central South University
Changsha, Hunan 410083, China

ready well understood. This option is being explored by researchers, including us, by incorporating the archetypal light-active linkage isomer fragment nitroprusside ($[Fe(CN)_5(NO)]^{2-}$, NP) into hybrid perovskite-like architectures. Historically studied as the sodium dihydrate salt (SNP), NP was known for some time to possess two photoinduced metastable states, MS_1 and MS_2,[7] but the structural basis for these unusually long-lived species remained elusive until the seminal photocrystallographic studies of Coppens et al. in 1997. In situ single-crystal X-ray diffraction (SCXRD) identified photoinduced linkage isomerism (PLI) from the ground state (η^1-NO) ligand to either the (η^1-ON) MS_1 or side-bound (η^2-ON) MS_2 depending on the conditions.[8] Now one of the most studied examples of PLI,[9] the structural and photophysical properties of NP are well-understood, which makes it a strong candidate for use as the basis for new multifunctional materials. Added attractions include the fact that Fe has lower toxicity than, for example, Pb, that SNP-based materials are comparatively low-cost, and can be synthesized from aqueous solution at low *T* and pressures.

By analogy with organic–inorganic perovskites, we focus on compounds of the formula $(A)[MFe(CN)_5(NO)].xH_2O$, where A is an ammonium cation and M a Group 1 metal, although other NP-based materials are also recently reported.[10] Early reports include the structure of $[(CH_3)_4N][NaFe(CN)_5(NO)].3.5H_2O$ in 1997.[11] More recently, the potential for NP frameworks to display cube-like structures analogous to perovskites, given a suitable A-site cation, was highlighted by the discovery of $[(CH_3)_2NH_2][KFe(CN)_5(NO)]$, which was found to display a near-room temperature (*RT*) symmetry-breaking phase transition.[12] Subsequent study of the related $[(CH_3)_2NH_2][NaFe(CN)_5(NO)]$ uncovered *RT* dielectric, piezoelectric and possible ferroelectric switching.[13] The authors also report the presence of the MS_1 and MS_2 isomers under 532 nm irradiation using in situ IR measurements. However, no photocrystallographic studies have yet been conducted to confirm these assignments. Recently, $[(CH_3)_2NH_2][CsFe(CN)_5(NO)]$ was reported to display dielectric switching, but no photoresponse was reported.[14] Finally, *T*-induced dielectric switching and NO photoswitching were reported for $(CH_3NH_3)[NaFe(CN)_5(NO)].H_2O$.[15] These studies show the promise of $(A)[MFe(CN)_5(NO)].xH_2O$ materials, but with some key outstanding questions. Most importantly, while the coexistence of photo- and field-induced responses has been demonstrated, no study has yet been able to ascertain if these are correlated. For a truly photoswitchable pyro- or ferroelectric system, it must be proven that irradiation induces the order-disorder response. As such, a better understanding of the mechanistic basis for each type of switching is required. This can be most effectively achieved using in situ studies, of which in situ SCXRD provides the most comprehensive information in the form of a series of 3D structures of the whole system at regular points during a switching event. Herein, we study a new formamidinium analogue, $(FA)[NaFe(CN)_5(NO)].H_2O$ (**1**) ($FA{=}NH_2(CH)NH_2^+$), via a combination of piezo-, pyro- and ferroelectric measurements, and in situ SCXRD including photocrystallography and novel *E*-cell experiments. We show that **1** displays *RT* piezo- and pyroelectricity, as well as *T*, *T*+*E* and photo-induced switching in the single-crystal, and use crystallographic insight to explore why no correlation between photo and dielectric effects is seen in such materials to-date.

Results and Discussion

1 was synthesized by combining equimolar amounts of FACl and $SNP.2H_2O$ in the minimum volume of 1:1 deionized water and methanol. Single-crystals were obtained by evaporation of the mother liquor. Crystal size and habit can be controlled by the speed of evaporation, with large, plate-like crystals obtained by slow evaporation and smaller prismatic needles obtained by drop-casting (Figure S1). For in situ SCXRD, needles with a reproducible size distribution were obtained by quenching the drop-cast crystallization solution with Fomblin Y-1800 oil after an appropriate growth period, monitored by optical microscopy. The identity of the product was confirmed by IR, CHN (SI, §1), and single-crystal and powder XRD.

At 273 K, the crystal structure of **1** solves in the orthorhombic *Cmcm* space group with Z'=0.25, i.e. the asymmetric unit consists of ¼ of a Na^+, FA^+ and NP^{2-} ion and ¼ of a coordinated H_2O molecule (Figure S2). $[Fe(CN)_5(NO)]^{2-}$ ions bridged by Na^+ form a cube-like anionic, polymeric framework, with FA^+ occupying the interstitial sites (Figure 1). The FA^+ sit jointly on the 2-fold axis parallel to [010] and the mirror plane parallel to [100], and are disordered at 273 K. A stable two-component model was refined with a 59(1):41(1) occupancy ratio. Capping with the NO and coordinated H_2O results in a layered structure composed of 2D sheets extending in the *a*-*c* plane. Excepting FA^+, **1** is isostructural with its MA^+ analogue near *RT*.[15] There is some ambiguity in the space group assignment, however, with the diffraction intensity statistics showing a slight preference for non-centrosymmetry (Figure S3) and $<E^2-1>=0.833$.[16] However, solution in the suggested $Cmc2_1$

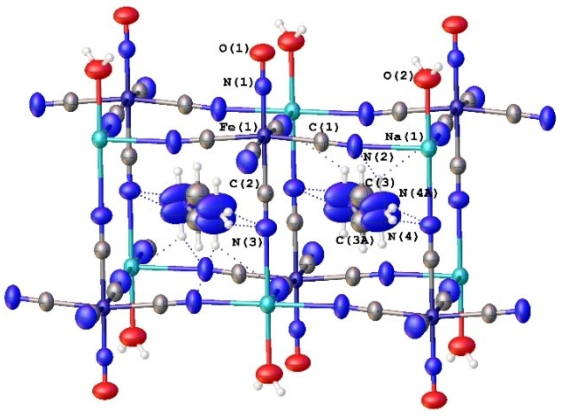

Figure 1. Extended single-crystal X-ray structure of **1** in the 273 K ground state, showing the perovskite-like framework and disordered FA^+ cations. Anisotropic displacement ellipsoids are set at 50% probability and hydrogen bonds are shown as red dashed lines.

setting as a racemic twin gives a Flack parameter[17] of 0.49(10) (Figure S4, Table S1), which by crystallographic convention indicates a centrosymmetric setting is preferable. Similarly, validation in PLATON[18] prefers *Cmcm*, indicating that this is the crystallographically correct space group. It should be noted however that SCXRD provides only the time- and space-averaged structure and thus cannot reliably elucidate any structure variations that occur faster than the total data collection time, or on length scales smaller than the crystal bulk.

Crystals of **1** were first assessed ex situ to test for piezo-, pyro- and ferroelectric responses. Either of the two crystal habits were used depending on the sample requirements for each measurement. To confirm the direction of the electric field (E) applied to the crystals, the real crystal faces for both habits were indexed using SCXRD. The large, flat faces of the plates index as (010) and (0–10) (Figure S5). For the needle habit, face-indexing confirms the long needle direction to be parallel with [001] (Figure S6). This detailed understanding of each crystal habit facilitated the application of E along specific crystal axes, most particularly along the potentially polar [001] direction.

The longitudinal piezoelectric charge coefficient (d_{33}) was measured by the direct piezoelectric effect method using a piezo-d_{33} meter (ZJ-4AN, Academic Sinica, China). Values of $d_{33}=1.3$ and 0.8 pC/N were measured from a fresh crystal and after poling, respectively, and indicate a piezoelectric response.

Polarization-Electric field (P-E) loops were next recorded on a plate-like crystal (Figure 2a). Due to the requirements of the analyzer, the field was applied along [010] in this case. The crystal exhibits a fully-reversible hysteretic loop in the region of $E=\pm 20\ \mathrm{kVcm^{-1}}$, but there is little evidence of polarization saturation at the maximum applied field. This is consistent with lossy capacitor behavior rather than a ferroelectric response.[19] A second series of P–E loops were also recorded on a ca. 1 mm-long needle-like crystal, this time with the field applied along the [001] direction. The crystal was mounted in a test cell to allow for good alignment with the field and facile electroding of the small (001) and (00–1) faces (Figure S7). The P-E loops again demonstrated a reversible hysteretic response but indicative of lossy capacitor behavior (Figure S8). The results are therefore not consistent with a ferroelectric response in **1** and indicate that the direction of the applied field does not influence the P–E hysteresis measurement.

The dielectric constant, ε' as a function of frequency and of T was next recorded from crystals of each habit, mounted in the same test cell and electroded at the (001) and (00–1) faces (Figure 2b and S9). Both habits showed an expected decrease in ε' with increasing frequency, and the values obtained are consistent with those determined for the isostructural MA analogue at *RT*.[15] The value of ε' varies little with T, showing a small decrease on cooling and concomitant increase on warming that is within error (Figure S10). As such, **1** shows no dielectric switching in response to T.

Finally, crystals of **1** were also subject to pyroelectric testing while mounted in the test cell and electroded at (001) and (00–1). T oscillations were generated by irradiating a crystal with a heat lamp and the current was measured using a Keithley 6514 electrometer. A reversible pyroelectric current in the picoamp range was measured over repeat heat/cool cycles (Figure 2c, S11), and visual inspection of the crystals before and after testing showed no change. Though the size of the current generated is not large, this is perhaps not unexpected given the small area of the single-crystal since:

$$I = p.A.\frac{dT}{dt}$$

where p is the pyroelectric coefficient, I is the short circuit pyroelectric current, A is the sample area ($\approx$1 cm^2) and dT/dt is the rate of change of T. The direction of the measured current was observed to change with heating and cooling cycles (Figure 2c), in agreement with the equation. A very approximate estimate of $p=1.0(7)\ \mu\mathrm{C/m^2\,^\circ C}$ was made from these data (SI §3) which is ca. 2 orders of magnitude smaller than that of archetypal pyroelectric lead zirconate titanate (PZT), though closer in value to others e.g. polyvinylidene fluoride (PVDF).[20] However, it should be noted that the errors in this measurement are large, resulting from the challenges of measuring such small I values with the equip-

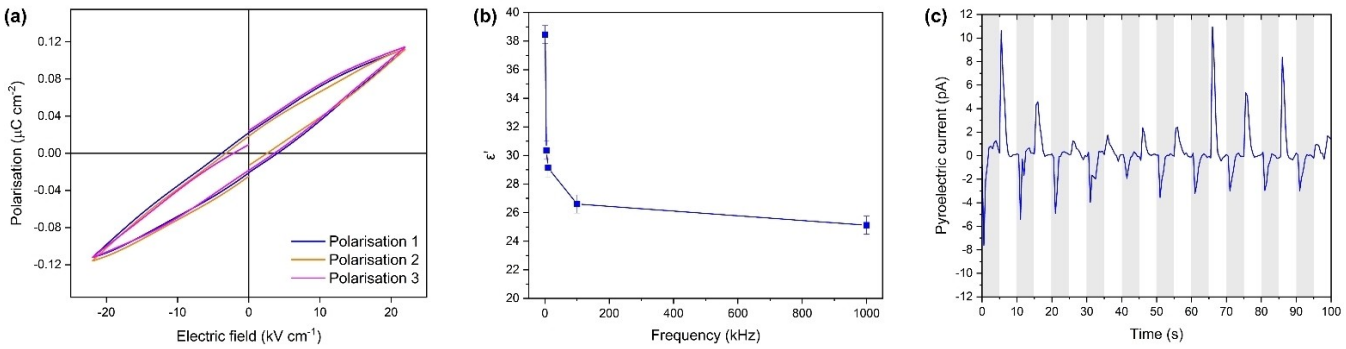

Figure 2. Ex situ testing on plate single crystals of **1**. (a) Polarisation—Electric field (P-E) loop testing between $E=\pm 20\ \mathrm{kVcm^{-1}}$. (b) Dielectric constant at *RT* as a function of frequency. (c) Pyroelectric current generated by repeated T oscillations created with a heat lamp, grey shading = lamp on, no shading = lamp off.

ment available (see Supporting Information §3), thus significant conclusions should not be drawn from the value of *p*.

Piezo- and pyroelectricity require a non-centrosymmetric and polar crystal class, respectively. As such, these properties of **1** do not correlate with the centrosymmetric bulk structure determined by SCXRD. Harmonic generation experiments were next conducted on **1** to further investigate its symmetry. Crystals of **1** displayed second harmonic generation (SHG) on probing at 1200 nm (Figure S12), as well as both SHG and third harmonic generation (THG) on probing at 1300 nm (Figure S13). These non-linear optical effects provide further evidence of non-centrosymmetry, agreeing with piezo- and pyroelectric properties.

In situ SCXRD experiments were next performed on needle-like crystals of **1** to characterize the structural changes in response to thermal, photochemical and electrical stimulation. First, a variable temperature (*VT*) study was run in which a crystal was cooled stepwise from 273–100 K, with cooling paused at regular intervals for data collection (Figure S15). In the absence of other stimuli, slow-cooling to 100 K results in a gradual ordering of the FA^+, approaching a fully-ordered structure by 120 K (Figure 3 and S16). The order-disorder transition is reversible on warming with a 10 K-wide hysteresis (Figure S17). During this transition the cube-like SNP framework is retained and the structure remains in the *Cmcm* space group, with all structures validated in PLATON.[18] However, the diffraction intensity ($I/\sigma(I)$) reduces below 150 K and new diffraction peaks appear between the Bragg reflections of the parent *Cmcm* cell along the *k*-direction in reciprocal space, indicating supercell formation (Figure S18). Due to the presence of these supercell peaks, the data reduction statistics for the low-temperature (*LT*) measurements in the parent *Cmcm* cell are unavoidably poorer compared to the near-*RT* measurements (Table 1). Unfortunately, the supercell reflections measured have very low $I/\sigma(I)$ values and attempts to refine the larger supercell structure from this data failed. A second *VT* cycle on the same crystal confirmed that the thermal behavior is reproducible within error. Interestingly, although the $I/\sigma(I)$ again reduced at *LT*, the presence of additional peaks was even less clear in the second cycle. *VT* PXRD measurements on a sample of powdered crystals (Figure S19) corroborate the absence of an abrupt (1st-order) *T*-induced phase transition, as inferred from the SCXRD measurements, with only subtle changes to the peak shape and splitting. A second set of *VT* experiments investigated the phase behavior of **1** at 300–500 K. Heating the crystal above *RT* causes no phase transformation, with only gradual changes in the unit cell parameters as expected on thermal expansion (Table S2, Figure S20). The *a* and *c* parameters do converge with increasing *T*, indicating a trend towards tetragonal symmetry, however they do not reach equality by 500 K. The only significant structure change on heating is the loss of the coordinated water molecule, which reduces to 20 % occupancy by 350 K and is eliminated by

Table 1: Single-crystal X-ray data for selected variable temperature (*VT*) and electric field (*E*)-cell measurements on **1**.

	Ground State (GS) structure	LTp structure +0 $kVcm^{-1}$ †	LTp structure +40 $kVcm^{-1}$ †
Mount type	Mitegen™ micromount	*E*-cell	*E*-cell
Empirical formula	$C_6H_7Fe_1N_8Na_1O_2$	$C_6H_7Fe_1N_8Na_1O_2$	$C_6H_5Fe_1N_8Na_1O_2$ *
Formula weight/kg mol^{-1}	302.04	302.04	300.02 *
Temperature/K	273	100	100
Radiation	Synchrotron (λ = 0.534 Å)	Synchrotron (λ = 0.534 Å)	Synchrotron (λ = 0.534 Å)
Crystal system	Orthorhombic	Orthorhombic	Monoclinic
Space group	*Cmcm*	*Cmcm*	*C*2/*m*
a/Å	7.6016(15)	7.4463(9)	19.4571(12)
b/Å	19.784(4)	19.4396(17)	7.5520(6)
c/Å	8.2281(16)	8.3227(9)	8.1295(5)
α/°	90	90	90
β/°	90	90	93.118(6)
γ/°	90	90	90
Volume/$Å^3$	1237.4(4)	1204.7(2)	1192.78(14)
Z	4	4	4
ρ_{calc}/g cm^{-3}	1.621	1.665	1.671
μ/mm^{-1}	0.577	0.593	0.598
F(000)	608.0	608.0	600.0 *
Crystal size/mm^3	0.1×0.03×0.03	0.1×0.03×0.03	0.1×0.03×0.03
Reflections (independent)	15069 (1059)	7596 (710)	8182 (6072)
Completeness	0.997	0.995	0.997
R_{int}	0.0335	0.2446	0.0986
R_1 [I > =2σ(I)]	0.0292	0.1015	0.0890
wR_2 [all data]	0.0798	0.2362	0.2494
Goodness-of-fit on F^2	1.048	1.053	1.010

* for the 100 K structure under applied field, the H atoms of the coordinated H_2O could not be modelled satisfactorily and are thus omitted from the final refinement.

† data quality for the *LT* structures are reduced compared to near-*RT* due to the presence of supercell reflections that appear on slow cooling, and due to the limitations imposed by the electric field cell apparatus, which additionally caused some icing at very low temperatures.

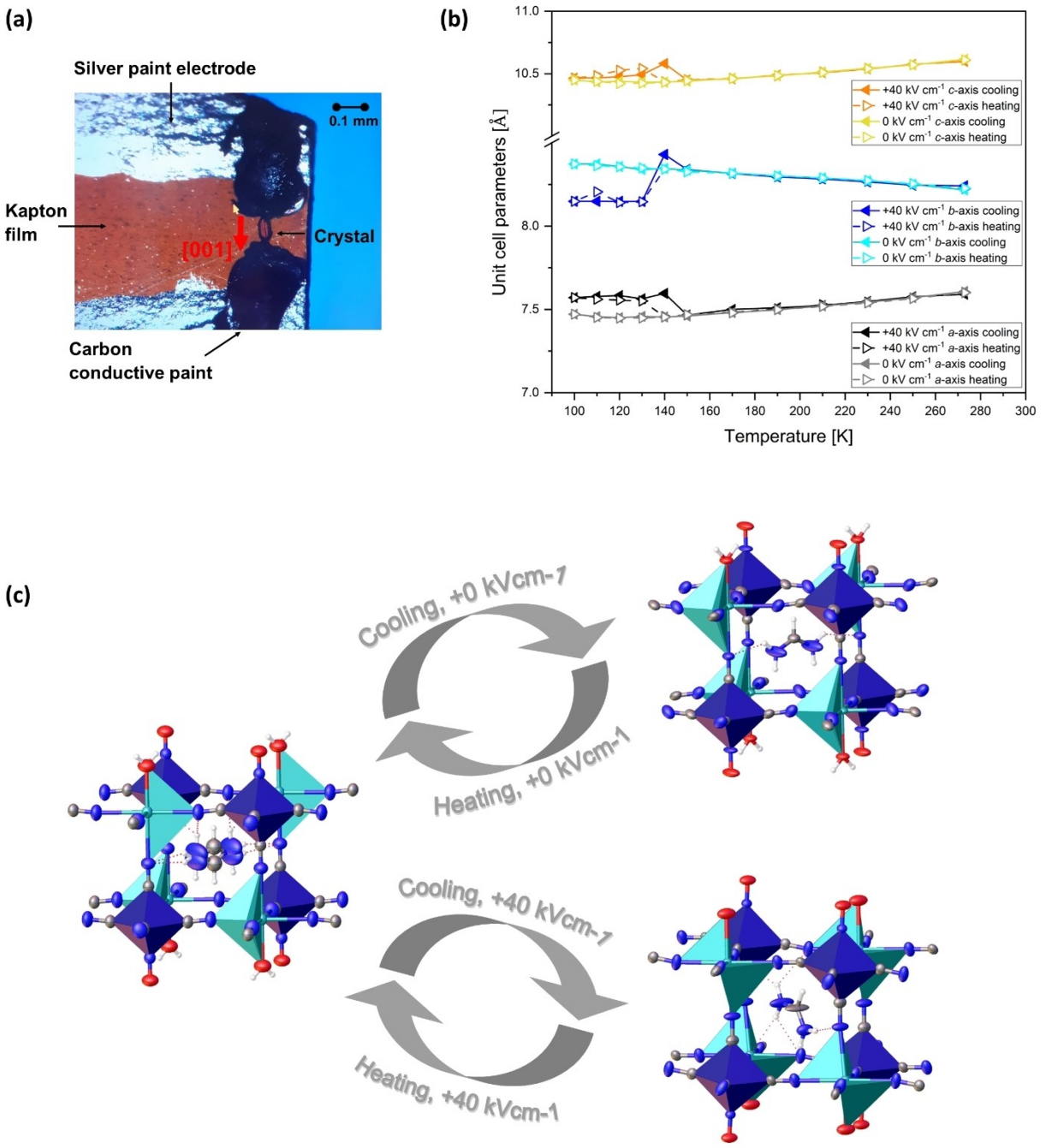

Figure 3. In situ single-crystal X-ray studies of **1**. **(a)** Microscope image of the *E*-cell loaded with a needle crystal of **1** with the unique [001] axis aligned to the field direction. **(b)** Reduced unit cell parameters as a function of *T* with $E = +40$ kVcm^{-1} and 0 kVcm^{-1}, showing a clear discontinuity at 150–140 K due to the phase transition. **(c)** In situ single-crystal X-ray data showing the change in structure on cooling with and without an applied field.

375 K. De-solvation proceeds without significant crystal degradation and diffraction is observed to 500 K. The *VT* SCXRD data are supported by differential scanning calorimetry (DSC) measurements at −50–200 °C, in which the de-solvation is observed in the first cycle (Figure S21).

We next performed in situ SCXRD studies under combined thermal and electrical stimulation, using a modified version of a published single-crystal *E*-cell apparatus.[21] A needle crystal was carefully aligned in the cell so that the (001) and (00–1) faces were electroded on the bespoke crystal mount (Figure 3a), and *VT* SCXRD experiments were run at $+40$ kVcm^{-1} and 0 kVcm^{-1}. The data at 0 kVcm^{-1} compare well to the standard *VT* SCXRD study, with gradual ordering of the FA^+ on cooling, retention of the *Cmcm* space group and a small hysteresis in the order-disorder transition (Figure S23). In contrast, cooling at

$+40\ kVcm^{-1}$ results in a drastic structural change, with a reversible phase transition to a monoclinic structure in *C*2/*m* at 140 K (Figure 3 and S22). To independently confirm the space group assignments through the $T+E$-induced phase transition, all data were first solved in the reduced cell (the unique primitive unit cell, based on the three shortest lattice translations) to remove any bias from imposed crystallographic symmetry, and the resulting *P*1 solutions were validated using the PLATON AddSym software.[18] The reduced cell parameters for the $+40\ kVcm^{-1}$ data show a discontinuity at the transition T with a small hysteresis, which is more prominent than in the $0\ kVcm^{-1}$ control measurement and confirms the phase transition (Figure 3b and S23). The symmetry-breaking transition results from tilting of the $[Fe(CN)_5(NO)]$ and $[Na(N)_5(H_2O)]$ octahedra, accompanied by a sudden ordering and significant shift in the position of the FA^+ (Figure S24 and S25). By analogy with M–X–M' perovskite tilts, the unique axial (Θ) and equatorial (Ω) [Fe–(CN)•–Na] angles were used to assess the magnitude of octahedral tilting, where (CN)• is the centroid of the CN bond. At the transition T with $+40\ kVcm^{-1}$, Θ abruptly switches from 180° to ca. 171°, while Ω changes from ca. 175° to 170.5°. The molecular dipoles of the FA^+, which are aligned along the [010] direction in the *Cmcm* phase, rotate by $\theta = 24°$ in the direction of the applied field (Figure S26). **1** fully reverts to the original *Cmcm* structure on warming above 130 K, with the crystal quality largely unaffected.

Finally, photocrystallographic studies were performed to identify any PLI. A needle crystal of **1** was confirmed to be in the parent *Cmcm* phase at *RT*, before being flash-cooled to 100 K and a ground-state (GS) structure (i.e. without illumination) was collected. Interestingly, the flash-cooled *LT* GS adopts an orthorhombic *Pnma* structure with double the unit cell volume of the step-cooled *Cmcm* phase (Figure 4, S27). Inspection of the diffraction pattern in reciprocal space shows the appearance of the supercell (Figure S28a), but comparison between this flash-cooled structure and the

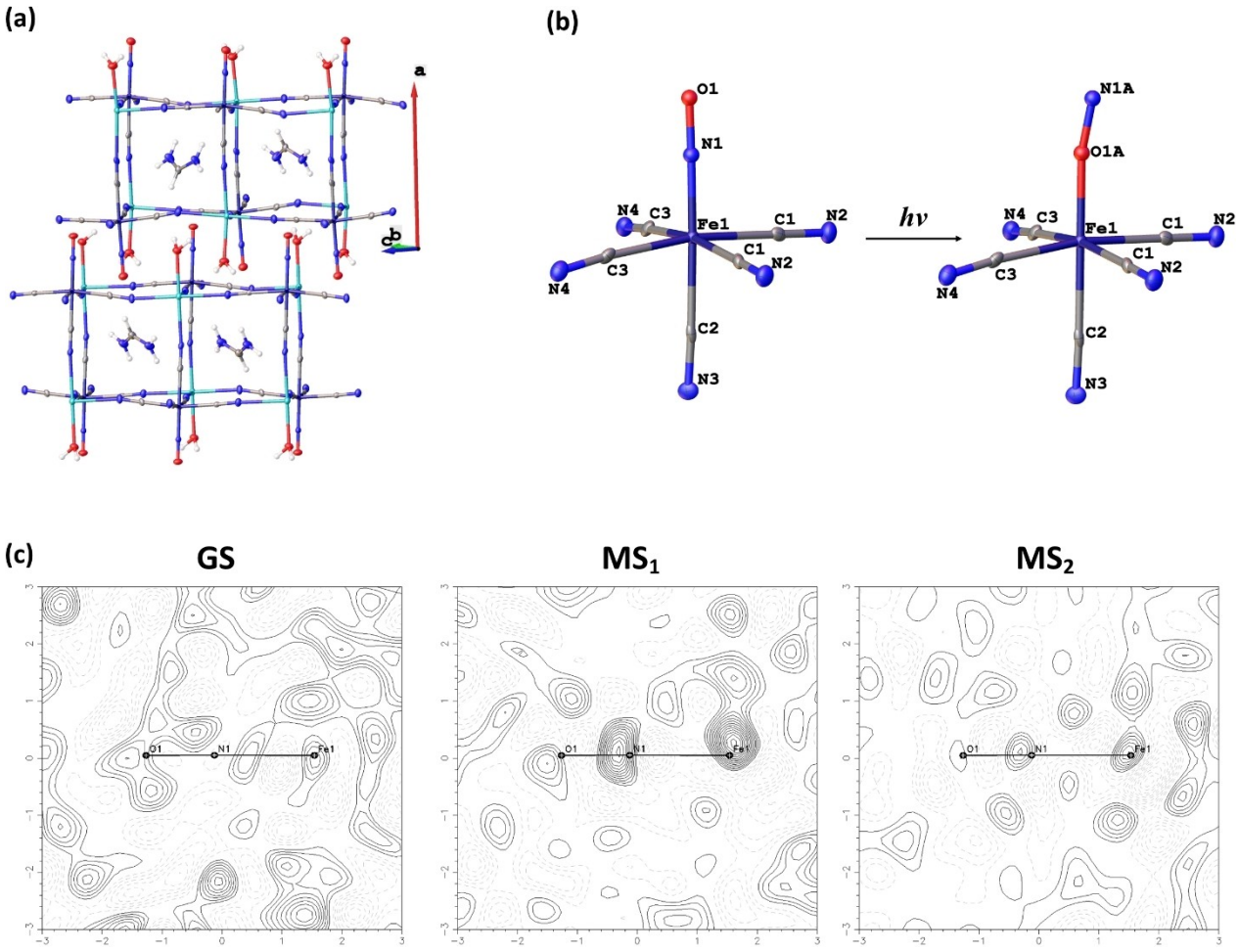

Figure 4. Photocrystallographic studies on **1**. **(a)** Packing diagram showing a portion of the flash-cooled 100 K *Pnma* structure of **1**. **(b)** Single-crystal X-ray structures of the photoactive NP^{2-} ion showing the GS (η^1-NO) and excited MS_1 (η^1-ON) arrangements in the Fe(1)–N(1)–O(1) moiety. **(c)** Fourier difference maps through the Fe(1)–N(1)–O(1) plane in the GS, MS_1 and MS_2 experiments. The GS map shows the residual density for the final GS model, while the MS_1 and MS_2 maps show the difference in residual density between a rigid-body refinement with the fixed GS coordinates and the photoexcited diffraction data (+ve contours = solid lines, -ve contours = dashed lines; contours set at +/−0.1 eA^{-3}; max/min difference density: GS = +0.88/−0.77 eA^{-3}, MS_1 = +1.45/−0.85 eA^{-3}, MS_2 = +0.71/−1.14 eA^{-3}).

100 K structure previously obtained by step-cooling shows a different pattern of supercell reflections (Figure S29). This indicates that the cooling rate influences the superstructure adopted by **1** at *LT*, an observation supported by the fact that it was not possible to re-solve the step-cooled 100 K data in this new *Pnma* supercell. The *Pnma* structure retains the cube-like framework but displays some tilting, with unique [Fe-(CN)•-Na] angles of 170.00°, 175.08° and 176.62° about Fe(1) and 170.11°, 175.86° and 178.60° about Fe(2) (Figure S30). The FA^+ are fully ordered and sit on the mirror plane parallel to [010]. To further investigate this new *LT* phase, the crystal was warmed step-wise back to 293 K, with heating paused and SCXRD data collected at intervals (Table S3). The *Pnma* phase reverts to the parent *Cmcm* structure between 140 and 160 K, confirmed by the disappearance of supercell peaks by 160 K (Figure S28).

A second crystal of **1** was flash-cooled, then held at 100 K and irradiated in situ for 90 min, using a bespoke LED array which positions 4×505 nm LEDs in a uniform arc at ca. 1 cm from the sample position (Figure S31), while being rotated about the φ-axis. PLI states are expected to be very long-lived (i.e. metastable) at *LT*, therefore the LEDs were switched off after the irradiation period and a second SCXRD dataset obtained in the absence of external light (Table 2). By creating a 'photodifference map' between the photoexcited dataset and the GS model coordinates,[22] difference peaks corresponding to the photoinduced (η^1-ON) MS_1 geometry were identified (Figure 4, S32) and MS_1 occupancies of 22 % and 26 % were refined for the two independent NO groups. Further irradiation at $\lambda = 505$ nm caused no further change. A second photocrystallographic study was run in an attempt to access the MS_2 isomer, where the same crystal in its MS_1 state was irradiated with near-IR (950 nm) LEDs for 60 min before collecting a third dataset.[8] This data is less conclusive: while there are peaks in the photodifference map that may correspond to a side-on (η^2-ON) isomer (Figure 4, S32), the lower residual density meant that a reasonable crystallographic model could not be found. Peaks corresponding to MS_1 were also still visible in the photodifference map, suggesting a mixture of states. It is likely that irradiation at 950 nm depopulates MS_1 towards both MS_2 and the GS, as seen previously,[8,9h] and thus MS_2 may be at such low occupancy that it is difficult to model accurately. GS→MS_1 PLI is fully reversible on warming the crystal above 160 K. The residual peaks in the photodifference map at $T \geq 180$ K are consistent with background difference density, confirming reversion to the GS (η^1-NO) isomer (Figure S33).

We now consider three discussion points arising from these in situ studies: (i) how does the structure of **1** allow for a piezo- and pyroelectric response; (ii) how does the application of *E* influence the phase transitions in **1**; and (iii) is there any evidence of correlation between the photo- and *T* and *E* responses?

Measurements indicate that **1** displays piezoelectricity, pyroelectricity, SHG and THG at *RT*. However, these properties require a non-centrosymmetric and polar crystal class, respectively, which is inconsistent with the crystallographically preferred *Cmcm* space group. The discrepancy may be reconciled by noting that SCXRD is a space-

Table 2: Single-crystal X-ray data for photocrystallographic studies on **1**.

	Flash-cooled GS structure	MS_1 experiment (505 nm irradiation)	MS_2 experiment (950 nm irradiation)
Irradiation time/min	0	90	60
Irradiation wavelength	n/a	505	950
Mount type	Mitegen™ micromount	Mitegen™ micromount	Mitegen™ micromount
Empirical formula	$C_6H_7Fe_1N_8Na_1O_2$	$C_6H_7Fe_1N_8Na_1O_2$	$C_6H_7Fe_1N_8Na_1O_2$
Formula weight/kg mol^{-1}	302.04	302.04	302.04
Temperature/K	100	100	100
Radiation	Mo Kα (λ = 0.71073)	Mo Kα (λ = 0.71073)	Mo Kα (λ = 0.71073)
Crystal system	Orthorhombic	Orthorhombic	Orthorhombic
Space group	*Pnma*	*Pnma*	*Pnma*
a/Å	38.635(4)	38.552(3)	38.553(2)
b/Å	8.3925(8)	8.3859(5)	8.3746(4)
c/Å	7.4335(8)	7.4314(5)	7.4200(4)
α/°	90	90	90
β/°	90	90	90
γ/°	90	90	90
Volume/Å^3	2410.3(4)	2402.5(3)	2395.7(2)
Z	8	8	8
ρ_{calc}/g cm^{-3}	1.665	1.670	1.675
μ/mm^{-1}	1.295	1.299	1.303
F(000)	1216	1216	1216
Crystal size/mm^3	0.3×0.1×0.1	0.3×0.1×0.1	0.3×0.1×0.1
Reflections (independent)	8863 (2627)	15899 (2626)	9686 (2617)
Completeness	0.995	0.997	0.995
R_{int}	0.0618	0.0584	0.0351
R_1 [I > =2σ(I)]	0.0475	0.0392	0.0328
wR_2 [all data]	0.1001	0.0967	0.0836
Goodness-of-fit on F^2	1.003	1.043	1.067

averaged technique, therefore the structure obtained from this analysis is a spatial average across the whole crystal and is not sensitive to any domain structure. It is therefore possible that the crystals of **1** comprise of randomly orientated $Cmc2_1$ domains that average to *Cmcm* across the crystal bulk. Spatially-resolved measurements, such as Raman mapping,[23] piezoelectric force microscopy[13] or scanning-electron microscopy,[24] may provide further insight. As SCXRD is also a time-averaged technique, it is also insensitive to any thermal or vibrational averaging occurring faster than the measurement timescale. To explore this further, and to address points (i) and (ii), the two *LT* phases obtained by cooling in the presence and absence of the electric field were investigated using structural-dynamics calculations[25] with density-functional theory (DFT; see SI, §7).

Classical inorganic ferroelectric materials, such as $BaTiO_3$, show a high-*T* paraelectric phase that undergoes one or more symmetry-lowering phase transitions to a ferroelectric phase with spontaneous polarization on cooling. The paraelectric phase is a low-lying maximum on the structural potential-energy surface linked through collective atomic displacements to two or more equivalent ferroelectric minima (possibly via a series of intermediate, lower-energy, maxima). At elevated *T*, sufficient thermal energy is available to access the paraelectric phase, which corresponds to what is effectively observed by spatially-averaged measurements such as SCXRD. On cooling, the atomic displacements are progressively "frozen in", ultimately confining the structure to one of the minima. If the displacements are uncorrelated, or correlated but over a small length scale, the *LT* phase typically consists of domains with randomly-oriented polarization, and the bulk crystal displays zero net polarization.[26] Application of an *E* alters the potential energy surface (PES) such that one of the minima is energetically preferred, which aligns most of the domains and produces a bulk net polarization. This can happen either at elevated *T* or on cooling, depending on the strength of the field and its interaction with the material relative to the thermal energy.

A key descriptor of these physics is the presence of imaginary harmonic modes in the phonon spectrum of the paraelectric phase, which identify a given phase as a local maximum on the PES and indicate the energy-lowering collective displacements toward the nearest local maxima/minima. For **1**, structural-dynamics calculations on the two optimised *LT* crystal structures obtained from the in situ *E*-cell study, *viz*. the 100 K structures at 0 $kVcm^{-1}$ and +40 $kVcm^{-1}$, which we label "*E*-OFF" and "*E*-ON", respectively, identified imaginary harmonic modes in the phonon spectra of both (see Supporting Information §7). The PES along the imaginary modes were then mapped to approximately locate the lower-energy structures associated with the modes (Figure S36), which were then optimised.[26–27] From the *E*-OFF structure, one of the five imaginary modes (Γ_1) led directly to a stable minimum with the *Cc* space group (Figure S37, Table S5). This structure is 4.81 $kJ\,mol^{-1}$ per F.U. lower in energy than the starting *E*-OFF structure and is the lowest energy of all the minima found in the PES search. For the *E*-ON structure, two of the six imaginary modes (Γ_1/Γ_4) led to distinct stable minima with the *C*2 space group (Figure S37, Table S5). These are 3.43 and 2.91 $kJ\,mol^{-1}$ per F.U., respectively, lower in energy than the starting *E*-ON structure but 1.89 and 2.41 $kJ\,mol^{-1}$ per F.U. higher than the *E*-OFF (Γ_1) minimum. However, a third mode (Γ_3) led to a maximum with a lower internal energy than both of these structures, and so the mapping process was repeated iteratively to eventually obtain a *P*-1 structure 4.94 $kJ\,mol^{-1}$ per F.U. lower in energy than the *E*-ON structure and just 0.38 $kJ\,mol^{-1}$ per F.U. higher in energy than the *E*-OFF (Γ_1) minimum (Figure S37, Table S5).

In an analogous manner to how our experimental data suggests that the near-*RT* *Cmcm* structure may be an average over lower-symmetry $Cmc2_1$ domains, these calculations suggest both the *Cmcm* structure and the *C*2/*m* structure obtained on cooling in an electric field are themselves averages over lower-symmetry structures. This supports the earlier observation that the SCXRD structures are time- and space-averages, and thus cannot account for observed properties of **1**. Of the four calculated minima, including the lowest-energy structure, three adopt non-centrosymmetric space groups (*C*2, *Cc*) and polar point groups (2, *m*). This indicates that **1** has a soft PES containing many closely-spaced minima, of which the majority adopt polar structures that would support piezo- and pyroelectricity and SHG behaviors, and this helps to explain the observed physical properties of **1**. Furthermore, the four minima are distinct, which suggests the structural PES from the *E*-ON and *E*-OFF structures are distinct, thereby demonstrating that applying an *E* during cooling can direct the crystal to explore a region of the PES that may not otherwise be accessible. Finally, comparing the minima with the starting structures further shows that the intricate PES revealed by these calculations is mediated primarily through the degrees of freedom of FA^+ and H_2O, but also by the flexibility of the host framework, which is evident from the minimal variation in the volume per F.U. across the different structures (Figure S37, Table S5).

We note here a few potential limitations of these calculations. The 100 K *E*-OFF structure was modelled in the $Cmc2_1$ setting, given the experimental evidence of piezo- and pyroelectricity. This resulted in small changes to the relative positions of the atoms in the starting unit cell, such that the higher *Cmcm* symmetry of the optimised structure could be recovered with a symmetry tolerance of 0.2 Å and is unlikely to be an issue. The disorder in the 273 K *RT* structure cannot easily be modelled in the calculations, and resolving it to the major component yielded an equivalent structure to the 100 K *E*-OFF model after geometry optimization. Given that standard DFT calculations are "athermal", and the inclusion of temperature effects would add further complications to treating the disorder, this is a necessary approximation. Finally, the partial PES search performed here cannot be guaranteed to locate the global minimum-energy structure, and it is possible there may be additional minima not found in the present study. However,

the cost of these calculations make it impractical to perform a more exhaustive mapping.

Finally, considering point (iii), photocrystallographic studies do not show any synergy between the photoswitching and the properties observed in response to *T* and applied *E*. NO is able to change coordination without causing any significant structure change to the framework or FA^+, indicating that the two switching behaviors are not correlated. This is supported by an assessment of the key intermolecular interactions between NO and the rest of the structure (Figure S34). The closest contacts are between the NO and neighboring CN groups, with a shortest distance of O(1)···N(7) = 3.062 Å. The most significant contacts are C–H···O hydrogen-bonds between the NO and neighbouring FA^+, e.g. C(10)–H(10A)···O(1) = 3.460 Å, which are categorized as weak, electrostatic-type interactions.[28] Thus, it is unsurprising that PLI can proceed without significantly altering the surrounding crystal structure. Similarly, measurement of the dielectric constant ε' as a function of irradiation time (Figure S35), indicates little correlation between the photo and dielectric properties, with no significant change in the ε' induced by illumination.

Conclusion

In conclusion, we have shown **1** to be a thermal, electrical and photoresponsive crystal that displays a complex series of structural transitions on exposure to different stimuli, including piezoelectricity, pyroelectricity, SHG and THG at *RT*. Structural-dynamics calculations suggest that the combined application of thermal and electrical stimuli can push the system into a new phase that is not otherwise accessible under ambient conditions. This work therefore highlights an effective route to manipulating material phase behavior under non-ambient conditions, potentially providing access to previously undiscovered phases with exploitable properties. Finally, this study shows that further engineering of these materials to "design-in" a correlated photo/electrical response is required, considering the proximity of switchable moieties in the crystal structure and their potential for significant interaction (e.g. via moderate-to-strong intermolecular contacts). Established crystal engineering principles (e.g. the rational incorporation of specific hydrogen/halogen-bond groups to target certain "supramolecular synthons",[29] size-matching of cations to the pores *etc.*) could all be helpful, and such approaches will be the focus of future studies.

Acknowledgements

L.E.H. and B.A.C. acknowledge funding from the Royal Society (URF\R1\191104). L.E.H also thanks Diamond Light Source for the award of beamtime to conduct the in situ VT and *E*-cell SCXRD experiments (beamtimes CY28436-1 and CY31624-1). J.J.M. is grateful to Cardiff University for PhD studentship support. PRR is grateful to the EPSRC for funding (EP/K004956/1). J.M.S. is currently supported by a UKRI Future Leaders Fellowship (MR/T043121/1) and previously held a University of Manchester Presidential Fellowship. The majority of the calculations were performed on the UK national ARCHER2 HPC facility, via J.M.S.'s membership of the UK Materials Chemistry Consortium (MCC), which is funded by the EPSRC (EP/R029431 and EP/X035859). C.B. and Q.W. acknowledge support of UKRI Frontier Research Guarantee on "*Processing of Smart Porous Electro-Ceramic Transducers—ProSPECT*", project EP/X023265/1. Y.Z. is grateful for support from the National Natural Science Foundation of China (No. 52302158). The authors thank Michael Zachariadis of the Imaging Facility at the University of Bath (doi.org/10.15125/mx6j-3r54), for their technical support and guidance in this work.

Conflict of Interest

The authors declare no conflicts of interest.

Data Availability Statement

The manuscript is accompanied by detailed Supporting Information available in PDF format, inclusive of computational data and methods. The authors have cited additional references within the Supporting Information. Deposition Numbers 2326867–2326893, 2327111–2327133 and 2339009–2339023 contain the supplementary crystallographic data for this paper. These data can be obtained free of charge from The Cambridge Crystallographic Data Centre and Fachinformationszentrum Karlsruhe via www.ccdc.cam.ac.uk/structures. Further experimental data are available via the Cardiff University Research Portal at http://doi.org/10.17035/d.2024.0313960534 and computational data are available at http://doi.org/10.17632/svtrf2g449.1.

Keywords: Phase transitions · Piezoelectric · Pyroelectric Photocrystallography · Nitrosyls

[1] a) O. Sato, *Nat. Chem.* **2016**, *8*, 644–656; b) M. A. Halcrow, *Spin-crossover materials: properties and applications*, John Wiley & Sons, **2013**; c) K. Dunbar, C. Achim, M. Shatruk, John Wiley & Sons: Oxford, UK, **2013**; d) H. Tsai, R. Asadpour, J.-C. Blancon, C. C. Stoumpos, O. Durand, J. W. Strzalka, B. Chen, R. Verduzco, P. M. Ajayan, S. Tretiak, J. Even, M. A. Alam, M. G. Kanatzidis, W. Nie, A. D. Mohite, *Science* **2018**, *360*, 67; e) M. Goulkov, D. Schaniel, T. Woike, *J. Opt. Soc. Am. B* **2010**, *27*, 927–932; f) M. Irie, T. Fukaminato, K. Matsuda, S. Kobatake, *Chem. Rev.* **2014**, *114*, 12174–12277; g) Y. Zhang, W. Zhang, S.-H. Li, Q. Ye, H.-L. Cai, F. Deng, R.-G. Xiong, S. D. Huang, *J. Am. Chem. Soc.* **2012**, *134*, 11044–11049; h) A. Z. Szeremeta, A. Nowok, S. Pawlus, K. Fedoruk, M. Trzebiatowska, M. Mączka, J. Symonowicz, M. Paluch, A. Sieradzki, *Applied Materials Today* **2021**, *22*, 100957.

[2] a) S. Manish, C. Aditya, V. Rahul, C. Vishal Singh, *Smart Mater. Struct.* **2015**, *24*, 105013; b) C. R. Bowen, J. Taylor, E. LeBoulbar, D. Zabek, A. Chauhan, R. Vaish, *Energy Environ.*

Sci. **2014**, *7*, 3836–3856; c) S. Gael, G. Daniel, A. Amen, *Smart Mater. Struct.* **2009**, *18*, 125006.
[3] a) M. Grätzel, *Acc. Chem. Res.* **2017**, *50*, 487–491; b) S. Han, M. Li, Y. Liu, W. Guo, M.-C. Hong, Z. Sun, J. Luo, *Nat. Commun.* **2021**, *12*, 284.
[4] a) Y. Rong, L. Liu, A. Mei, X. Li, H. Han, *Adv. Energy Mater.* **2015**, *5*; b) M. Grätzel, *Nat. Mater.* **2014**, *13*, 838–842; c) W. Ke, M. G. Kanatzidis, *Nat. Commun.* **2019**, *10*, 965.
[5] B. Yang, W. Ming, M.-H. Du, K. Keum Jong, A. Puretzky Alexander, M. Rouleau Christopher, J. Huang, B. Geohegan David, X. Wang, K. Xiao, *Adv. Mater.* **2018**, *30*, 1705801.
[6] A. A. Zhumekenov, M. I. Saidaminov, O. F. Mohammed, O. M. Bakr, *Joule* **2021**, *5*, 2027–2046.
[7] U. Hauser, V. Oestreich, H. D. Rohrweck, *Zeitschrift für Physik A Hadrons and Nuclei* **1977**, *280*, 17–25.
[8] M. D. Carducci, M. R. Pressprich, P. Coppens, *J. Am. Chem. Soc.* **1997**, *119*, 2669–2678.
[9] a) N. Casaretto, D. Schaniel, P. Alle, E. Wenger, P. Parois, B. Fournier, E.-E. Bendeif, C. Palin, S. Pillet, *Acta Crystallogr. Sect. B* **2017**, *73*, 696–707; b) Z. Tahri, R. Lepski, K.-Y. Hsieh, E.-E. Bendeif, S. Pillet, P. Durand, T. Woike, D. Schaniel, *Phys. Chem. Chem. Phys.* **2012**, *14*, 3775–3781; c) M. S. Lynch, M. Cheng, B. E. Van Kuiken, M. Khalil, *J. Am. Chem. Soc.* **2011**, *133*, 5255–5262; d) G. Gallé, M. Nicoul, T. Woike, D. Schaniel, E. Freysz, *Chem. Phys. Lett.* **2012**, *552*, 64–68; e) V. Dieckmann, M. Imlau, D. H. Taffa, L. Walder, R. Lepski, D. Schaniel, T. Woike, *Phys. Chem. Chem. Phys.* **2010**, *12*, 3283–3288; f) A. Klein, Y. v. Mering, A. Uthe, K. Butsch, D. Schaniel, N. Mockus, T. Woike, *Polyhedron* **2010**, *29*, 2553–2559; g) D. Schaniel, M. Nicoul, T. Woike, *Phys. Chem. Chem. Phys.* **2010**, *12*, 9029–9033; h) D. Schaniel, T. Woike, *Phys. Chem. Chem. Phys.* **2009**, *11*, 4391–4395; i) D. Schaniel, T. Woike, C. Merschjann, M. Imlau, *Phys. Rev. B* **2005**, *72*, 195119; j) T. Woike, S. Dahaoui, D. Schaniel, S. Ponou, K. Hansen Niels, V. Petricek, *Zeitschrift für Kristallographie/ International journal for structural, physical, and chemical aspects of crystalline materials* **2004**, *219*, 558; k) D. Schaniel, J. Schefer, B. Delley, M. Imlau, T. Woike, *Phys. Rev. B* **2002**, *66*, 085103.
[10] W.-J. Xu, M.-F. Li, A. R. Garcia, K. Romanyuk, J. M. G. Martinho, P. Zelenovskii, A. Tselev, L. Verissimo, W.-X. Zhang, X.-M. Chen, A. Kholkin, J. Rocha, *J. Am. Chem. Soc.* **2023**, *145*, 13663–13673.
[11] J. J. Longridge, J. M. Rawson, J. E. Davies, *Acta Crystallogr. Sect. C* **1997**, *53*, 15–17.
[12] R.-G. Qiu, X.-X. Chen, R.-K. Huang, D.-D. Zhou, W.-J. Xu, W.-X. Zhang, X.-M. Chen, *Chem. Commun.* **2020**, *56*, 5488–5491.
[13] W.-J. Xu, K. Romanyuk, J. M. G. Martinho, Y. Zeng, X.-W. Zhang, A. Ushakov, V. Shur, W.-X. Zhang, X.-M. Chen, A. Kholkin, J. Rocha, *J. Am. Chem. Soc.* **2020**, *142*, 16990–16998.
[14] Q.-Y. Li, M.-F. Li, X.-X. Chen, Y.-P. Gong, D.-X. Liu, W.-J. Xu, W.-X. Zhang, *CrystEngComm* **2022**, *24*, 4864–4868.
[15] Y.-X. Li, X.-L. Wang, Y. Li, O. Sato, Z.-S. Yao, J. Tao, *Inorg. Chem.* **2021**, *60*, 380–386.
[16] A. J. Blake, W. Clegg, J. M. Cole, *Crystal structure analysis: principles and practice*, Oxford University Press, **2009**.
[17] H. D. Flack, G. Bernardinelli, *Acta Crystallogr. Sect. A* **1999**, *55*, 908–915.
[18] A. Spek, *J. Appl. Crystallogr.* **2003**, *36*, 7–13.
[19] M. Stewart, M. Cain, D. Hall, *Report CMMT (A)* **1999**, *152*.
[20] a) Y. Zhang, M. Xie, J. Roscow, Y. Bao, K. Zhou, D. Zhang, C. R. Bowen, *J. Mater. Chem. A* **2017**, *5*, 6569–6580; b) R. W. Whatmore, *Rep. Prog. Phys.* **1986**, *49*, 1335.
[21] L. K. Saunders, H. H.-M. Yeung, M. R. Warren, P. Smith, S. Gurney, S. F. Dodsworth, I. J. Vitorica-Yrezabal, A. Wilcox, P. V. Hathaway, G. Preece, P. Roberts, S. A. Barnett, D. R. Allan, *J. Appl. Crystallogr.* **2021**, *54*, 1349–1359.
[22] P. Coppens, M. D. Carducci, K. Culp, D. Fomitchev, *Abstr. Pap. Am. Chem. Soc.* **1997**, *214*, 318-INOR.
[23] G. F. Nataf, N. Barrett, J. Kreisel, M. Guennou, *J. Phys. Condens. Matter* **2018**, *30*, 035902.
[24] K. A. Hunnestad, E. D. Roede, A. T. J. van Helvoort, D. Meier, *J. Appl. Phys.* **2020**, *128*.
[25] a) A. Togo, I. Tanaka, *Scr. Mater.* **2015**, *108*, 1–5; b) K. Parlinski, Z. Q. Li, Y. Kawazoe, *Phys. Rev. Lett.* **1997**, *78*, 4063–4066.
[26] W. Rahim, J. M. Skelton, C. N. Savory, I. R. Evans, J. S. O. Evans, A. Walsh, D. O. Scanlon, *Chem. Sci.* **2020**, *11*, 7904–7909.
[27] J. M. Skelton, L. A. Burton, S. C. Parker, A. Walsh, C.-E. Kim, A. Soon, J. Buckeridge, A. A. Sokol, C. R. A. Catlow, A. Togo, I. Tanaka, *Phys. Rev. Lett.* **2016**, *117*, 075502.
[28] G. A. Jeffrey, *An Introduction to Hydrogen Bonding*, Oxfor University Press, **1997**.
[29] G. R. Desiraju, *Chem. Commun.* **1997**, 1475–1482.

Manuscript received: January 23, 2024
Accepted manuscript online: March 18, 2024
Version of record online: ■■, ■■

Research Articles

Photocrystallography

J. J. Morris, C. R. Bowen, B. A. Coulson, M. Eaton, P. R. Raithby, L. K. Saunders, J. M. Skelton, Q. Wang, M. R. Warren, Y. Zhang, L. E. Hatcher* **e202401552**

Exploring Pyroelectricity, Thermal and Photochemical Switching in a Hybrid Organic-Inorganic Crystal by In Situ X-Ray Diffraction

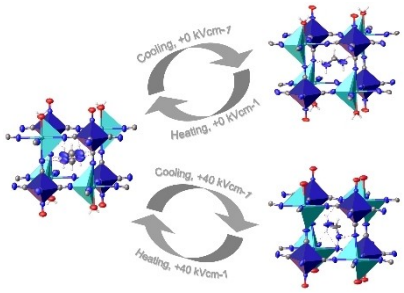

Hybrid materials based on known molecular photoswitches show great potential for the rational design of new pyro- and ferroelectric photoswitches. This article shows how in situ X-ray diffraction using thermal, photochemical and electrical stimuli can explore structure–property relationships in the novel pyroelectric (FA)[NaFe(CN)$_6$(NO)].H_2O, enabling a deeper understanding of its complex energy landscape via structural-dynamics calculations.